

pubs.acs.org/JPCL Letter

Condensed Phase Water Molecular Multipole Moments from Deep Neural Network Models Trained on *Ab Initio* Simulation Data

Yu Shi, Carrie C. Doyle, and Thomas L. Beck*



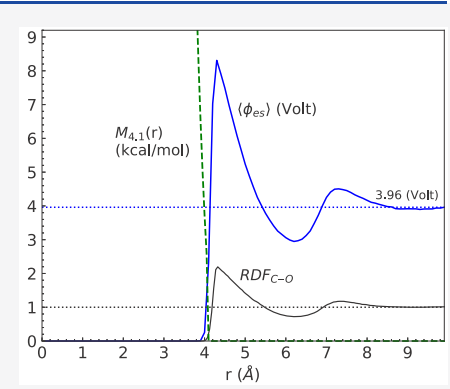
Cite This: J. Phys. Chem. Lett. 2021, 12, 10310-10317



ACCESS

III Metrics & More

ABSTRACT: Ionic solvation phenomena in liquids involve intense interactions in the inner solvation shell. For interactions beyond the first shell, the ion—solvent interaction energies result from the sum of many smaller-magnitude contributions that can still include polarization effects. Deep neural network (DNN) methods have recently found wide application in developing efficient molecular models that maintain near-quantum accuracy. Here we extend the DeePMD-kit code to produce accurate molecular multipole moments in the bulk and near interfaces. The new method is validated by comparing the DNN moments with those generated by *ab initio* simulations. The moments are used to compute the electrostatic potential at the center of a molecular-sized hydrophobic cavity in water. The results show that the fields produced by the DNN models are in quantitative agreement with the AIMD-derived values. These efficient methods will open the door to more accurate solvation models for large solutes such as proteins.



In a liquid electrolyte mixture, interactions between a solute ion and first-shell solvent molecules can be of significant magnitude. The electric fields acting on the nearby solvent molecules can reach magnitudes as large as several V/Å. Such fields are certain to create significant charge distortions in the surrounding solvent molecules. It can thus be expected that the inner-shell interactions will display nonlinear characteristics, and they will be highly ion- or molecule-specific. Computations of ion hydration entropies support this point of view: ion specificity in the entropy arises almost entirely from near-local interactions in the first hydration shell.

Outside of the first hydration shell, the solute—solvent interaction energies are due to a large number of smaller-magnitude contributions, which can often be approximated at the Gaussian (or linear-response) level. These interactions can include substantial contributions from electronic polarization. In addition, a uniform shift in the free energies has been observed in classical simulations, independent of ion size but depending on the charge. This is a clear indication of an electric field due to local inhomogeneous solvent distributions near the cavity. It is the physical origin of this shift that is the focus of the present study.

The quasi-chemical theory (QCT)^{12,13} provides an exact and physically insightful spatial partitioning of the free energy into terms involving the following processes: (1) cavity formation, (2) long-range free energy due to inserting the solute into the cavity, and (3) relaxation of the cavity constraint that produces the inner-shell free energy due to the above-discussed intense interactions.¹⁴ The above 3-step

process can be reorganized into a form for the excess chemical potential μ^{ex} that motivates the quasi-chemical appellation: ¹³

$$\mu^{\text{ex}} = -kT \ln K_n^{(0)} \rho_{\text{W}}^n + kT \ln p(n) + \mu_{XW_n}^{\text{ex}} - n\mu_{\text{W}}^{\text{ex}}$$
(1)

Article Recommendations

Here k is Boltzmann's constant, T the temperature, $K_n^{(0)}$ an equilibrium constant for assembling a cluster consisting of the solute and n solvent molecules in the gas phase, ρ_W the number density of solvent molecules (assumed to be water), p(n) the probability of observing n solvent molecules in the chosen inner-shell observation volume, $\mu_{XW_n}^{ex}$ the free energy to insert the assembled cluster into the solvent, and μ_W^{ex} the free energy to insert a solvent molecule into the solvent.

This partitioning of the free energy allows for helpful approximations when modeling solvation. For example, the first chemical-type term above can be evaluated with accurate quantum chemical techniques. The next term is typically quite small. The third term involves interactions of the inner-shell solute—solvent cluster with the more distant solvent. The resulting Gaussian behavior discussed above at longer-range is equivalent to a dielectric continuum model such as the Born model (with the exception of any potential shift, linear in the

Received: July 19, 2021 Accepted: October 14, 2021



charge, due to molecular distributions at interfaces). We note that the second peak in the radial distribution function (rdf) corresponding to the second solvation shell (around monatomic ions) occurs in the size range of 4–5 Å, which indicates the relevant cavity size for inserting the inner-shell XW_n -cluster.

We have recently examined interfacial potential effects related to determining a free energy scale for single-ion solvation. 11,15-19 These studies have included both classical and quantum molecular dynamics simulations coupled with the QCT.¹⁹ It has been shown that the net potential shift upon passing from the vacuum into a large water droplet and then into a molecular cavity provides a good measure of the longerranged electrostatic effects on ion hydration.¹⁸ (There are a significant size dependence and indications of nonlinear effects for smaller cavities.²⁰) The resulting potential shift due to longranged interactions, here and elsewhere estimated to be about -0.4 V, can potentially have important physical effects near interfaces, including alterations of ion distributions, water acid-base changes, and impacts on chemical reactions near the interface.21-23 The results obtained in the present study are consistent with the several alternative approaches discussed above.

Our previous classical study¹⁸ examined the role of water molecular dipolar and quadrupolar contributions to the interfacial potentials near the solute and at the distant liquid-vapor interface. The results highlighted the importance of the molecular quadrupole in determining the potential shift. It is important to utilize accurate solvent molecular charge distributions that are consistent with the realistic quantum mechanical multipole moment values, however, to make quantitative predictions of interfacial potential shifts at interfaces. Ab initio density functional theory simulations satisfy this requirement but are restricted in the length and time scales that are accessible. To overcome these limitations, deep learning methods have recently been successfully applied to the accurate modeling of water and other materials. 24-28 The impressive results show that much larger systems can be modeled with quantum-level accuracy but at the cost of classical simulations.

In order to go beyond simple classical fixed-charge models, herein we apply and extend existing deep learning techniques (the DeePMD-kit code²⁵) with an aim toward modeling the molecular multipole moments for water near molecular-sized cavities and in the bulk. 29,30 We then use the predicted dipoles and quadrupoles to provide an estimate of the net potential that we previously obtained 18 using the multipoles from the classical SPC/E water model, and we compare the results with our recent ab initio determination of the free energy scale for single-ion hydration.¹⁹ This step leading to the accurate yet efficient modeling of interfacial potential effects is crucial, because viable models of interfacial charge transfer that include the double layer, for example related to chemical catalysis, require treatment of large systems beyond the capability of direct AIMD methods. We note that, because the Wannier functions modeled in our work in principle produce the exact electron density, the results approximately include contributions from both polarization and charge transfer.

The excess chemical potential for an ion X is given by the Widom formula¹²

$$\mu_X^{\text{ex}} = -kT\ln\langle e^{-\varepsilon_X/kT}\rangle_0 \tag{2}$$

where ε_X is the interaction energy of the ion with the solvent and the subscript 0 indicates that there is no interaction between the ion and the solvating water molecules during the averaging process. The traditional expression for the electrochemical potential^{31,32} of the ion is

$$\mu_X^{\text{ex}} = \mu_{X,\text{bulk}}^{\text{ex}} + q_X \phi_{\text{np}} \tag{3}$$

where $\mu_{X,\text{bulk}}^{\text{ex}}$ is the free energy deep in the liquid phase with no electrostatic contribution from interfaces. We recently employed the quasi-chemical theory $(QCT)^{12,19}$ and AIMD simulations to compute the bulk hydration free energy of the Na⁺ ion.¹⁹

If the interaction energies are computed through simulations under periodic boundary conditions, we can view the free energy as

$$\mu_X^{\text{ex}} = \mu_{X,\text{int}}^{\text{ex}} + q_X \phi_{\text{sp}} \tag{4}$$

where $\mu_{X,\rm int}^{\rm ex}$ is the intrinsic chemical potential and $\phi_{\rm sp}$ is the liquid–vapor surface potential, which can be calculated from the total charge density profile through the interface. Then the net potential is defined as

$$\phi_{\rm np} = \phi_{\rm lp} + \phi_{\rm sp} \tag{5}$$

where ϕ_{lp} is the local potential that involves the electrostatic potential at the center of a molecular hydrophobic cavity in water.

In the QCT, the excess free energy is partitioned into three physical parts¹¹

$$\mu_X^{\text{ex}} = -kT \ln \langle e^{-M_{\lambda}/kT} \rangle_0 - kT \ln \langle e^{-\varepsilon_{\chi}/kT} \rangle_{M_{\lambda}} + kT \ln \langle e^{-M_{\lambda}/kT} \rangle_{\varepsilon_{\chi}}$$
(6)

Here M_{λ} is a repulsive potential pushing solvent molecules away to the distance λ ; the first term (packing, PK) is the free energy change to grow a cavity of radius λ in the liquid; the second term (long-ranged, LR) is the free energy change for inserting the ion into the cavity center; and the last term (inner-shell, IS) is minus the free energy change to grow the same cavity in the liquid around the ion. The interfacial potential contribution to the free energy resides in the second term (LR), for which the cumulant expansion is

$$\mu_{X,LR}^{\text{ex}} = -kT \ln \langle e^{-\varepsilon_X/kT} \rangle_{M_{\lambda}}$$

$$\approx \langle \varepsilon_X \rangle_{M_{\lambda}} - \frac{1}{2kT} \langle \delta \varepsilon_X^2 \rangle_{M_{\lambda}} + \frac{1}{6(kT)^2} \langle \delta \varepsilon_X^3 \rangle_{M_{\lambda}} + \dots$$
(7)

where $\delta \varepsilon_X = \varepsilon_X - \langle \varepsilon_X \rangle_{M_\chi}$ is the deviation of the interaction energy ε_X from the mean. The interaction energy can be partitioned as $\varepsilon_X = q\phi + \varepsilon_{\rm ind} + \varepsilon_{\rm disp}$, where ϕ is the net potential from the molecular charge distributions unperturbed by the ion, $\varepsilon_{\rm ind}$ the ion-induced-dipole induction interaction, and $\varepsilon_{\rm disp}$ the ion–water dispersion interaction. The dispersion term is expected to be small for large cavities, especially for the case of cations. The induction energy term is not included in the interfacial potential contribution because it is proportional to q^2 .

In simulations during which the electrostatic interactions are evaluated using Ewald summation with conducting boundary conditions, the integral of the electrostatic potential over the periodic box is zero.³⁴ We account below for the resulting shift

of the average potential on the cell boundary relative to an expected value of zero outside of the liquid sample at infinity (herein termed the Ewald-shift).

Previous studies have investigated multipolar contributions to interfacial potentials. ^{18,29,33} In the study of Horváth et al., ²⁹ the cavity potential $\langle \phi \rangle_{M(\lambda)}$ is constructed as

$$\langle \phi \rangle_{M_{\lambda}} = (-1)[\delta \phi_{D}(r) + \delta \phi_{Q1}(r) + \delta \phi_{Q2}(r)] \tag{8}$$

The dipole moment contribution to the cavity potential $\delta\phi_{\rm D}$ is determined from the dipole moment density $P_r(r)$

$$\delta\phi_{\rm D}(r) = \frac{1}{4\pi\epsilon_0} \int_0^r \frac{4\pi r'^2 P_r(r')}{r'^2} dr'$$
 (9)

The quadrupole moment contribution to the cavity potential $\delta\phi_{Q1}(r)$ is accessible from the simulation data via the radial dependence of the quadrupole moment density written in spherical coordinates

$$\delta\phi_{Q1}(r) = -\frac{1}{4\pi\epsilon_0} \frac{4\pi r^2 Q_{rr}^s(r)}{r^2}$$
(10)

where $Q_{rr}^{s}(r)$ is the radial element. In the bulk liquid water phase, it is equal to the Bethe potential:³⁵

$$\phi_{\rm B} = -\frac{1}{3\epsilon_0} \rho_{\rm W} \text{TrQ} \tag{11}$$

where the bulk water number density is $\rho_{\rm W}$ and Q is the water molecular primitive quadrupole moment as shown below. The second quadrupole contribution $\delta\phi_{\rm Q2}(r)$ is due to symmetry breaking of the quadrupole diagonal elements of the water in the vicinity of the cavity interface:

$$\delta\phi_{Q2}(r) = \frac{1}{4\pi\epsilon_0} \int_0^r \frac{4\pi r'^2 [TrQ(r') - 3Q_{rr}^s(r')]}{r'^3} dr'$$
(12)

We regard each water molecule as a neutral entity and use the following expression³⁶ to calculate the mth water molecular dipole moment

$$\mathbf{P}_{m} = \int_{\text{cell}} d\mathbf{r} \rho_{e}(r)(-2)\mathbf{r} + \sum_{i} Z_{i} \mathbf{R}_{i}$$
(13)

where $\rho_e(r)$ is the valence electron density function, \mathbf{Z}_i is the *i*th atom charge, and \mathbf{R}_i is the *i*th atom position of the molecule. The *m*th water molecular primitive quadrupole moment is given by³⁶

$$Q_{m,\mu\nu} = \frac{1}{2} \int_{\text{cell}} d\mathbf{r} \rho_e(r) (-2) (r_{\mu} r_{\nu}) + \frac{1}{2} \sum_i Z_i \mathbf{R}_{i,\mu} \mathbf{R}_{i,\nu}$$
(14)

and the *m*th water molecular traceless quadrupole moment³⁶ is given by

$$Q'_{m,\mu\nu} = \frac{1}{2} \int_{\text{cell}} d\mathbf{r} \rho_e(r) (-2) (3r_{\mu}r_{\nu} - \delta_{\mu\nu}r^2) + \frac{1}{2} \sum_i Z_i (3\mathbf{R}_{i,\mu}\mathbf{R}_{i,\nu} - \delta_{\mu\nu}\mathbf{R}_i^2)$$
(15)

The Wannier center of the *n*th MLWF, r_n , is given by

$$\langle r_{n,\mu} \rangle = \frac{L}{2\pi} \operatorname{Im}(\ln \langle \phi_n | e^{i2\pi/Lr_{\mu}} | \phi_n \rangle)$$
(16)

The electron quadrupole moment elements are then given by³⁷

$$\langle r_{\mu}r_{\nu}\rangle_{n} = \langle r_{\mu}\rangle_{n}\langle r_{\nu}\rangle_{n} + \frac{L^{2}}{16\pi^{2}}\{\ln|\langle\phi_{n}|e^{i2\pi/Lr_{\mu}}e^{-i2\pi/Lr_{\nu}}|\phi_{n}\rangle|^{2} - \ln|\langle\phi_{n}|^{i2\pi/Lr_{\mu}}e^{i2\pi/Lr_{\nu}}|\phi_{n}\rangle|^{2}\}$$

$$(17)$$

To maintain consistency with our previous classical study, 18 we take the oxygen atom as the water molecule center. Then the quadrupole elements with respect to the oxygen position \mathbf{R}_{o} are

$$\langle r_{\mu}^{o} r_{\nu}^{o} \rangle_{n} = \langle r_{\mu} r_{\nu} \rangle_{n} - R_{o,\mu} \langle r_{\nu} \rangle_{n} - R_{o,\nu} \langle r_{\mu} \rangle_{n} + R_{o,\mu} R_{o,\nu}$$
(18)

In reference to the point infinitely far away in the vacuum region, the potential at the cavity center can be expressed as 18

$$\langle \phi \rangle_{M_{\lambda}} = \sum_{m} \left[q_{m} \frac{1}{r_{m}} - P_{m,\mu} \nabla_{\mu} \frac{1}{r_{m}} + \frac{1}{3} Q'_{m,\mu\nu} \nabla_{\mu} \nabla_{\nu} \frac{1}{r_{m}} + \cdots \right]$$
(19)

where the summation is over all the water molecules; r_m is the mth water molecule's origin distance to the cavity center, and q_m is 0 because each water molecule is charge neutral.

Below, we first investigate the dipole and quadrupole moments from AIMD simulations to compare with experimental values and previous reports. Next, we show that the DNN-MD simulations accurately reproduce the distributions of the moment elements determined by AIMD. Finally, we show that the local potential from DNN-MD simulations is in reasonable agreement with that from AIMD simulations. The computational methodology is discussed at the end of the Letter.

Previous ground-breaking DNN modeling of the dielectric properties of water has shown that, for physical quantities requiring only the dipolar contribution, the Wannier center is the appropriate target of the deep learning algorithm. Those simulations have produced accurate models of the IR and Raman spectra of water. Equation 17 shows, however, that information beyond the Wannier centers is required for modeling the quadrupole moments. Thus, in the following we develop DNN methods to treat both the dipoles and quadrupoles.

Listed in Table 1 are the multipole-moments for the water monomer, water molecules near the cavity of 4.1 Å in the condensed phase, and water molecules in the neat liquid phase. For the water monomer in the simulation box of size L =12.4295 Å, the oxygen atom position is (2.9340, 2.0000, 3.0000); the first hydrogen's position is (H1, 3.5292, 1.2320, 3.0000), and the second hydrogen's position is (H2, 3.5292, 2.7680, 3.0000). With the water oxygen atom as the origin, the water molecular local coordinate system is defined by en the interior bisector of the angle H₁-O-H₂, the norm direction of the water molecular plane $\mathbf{e}_z = \mathbf{OH}_1 \times \mathbf{OH}_2$ and $\mathbf{e}_v = \mathbf{e}_z \times \mathbf{e}_x$. In the local frame, the water atomic dipole moment is 5.72 D and the water valence electronic dipole moment is -3.88 D, resulting in the dipole moment 1.84 D for the water monomer, which is in good agreement with the value 1.86 D from MP2 calculations and experimental observation. In the work by Silvestrelli and Parrinello,⁴² using DFT theory with the BLYP functional in a box of size L = 10.6 Å, the dipole moment is computed as 1.87 D. Finite-size effects have been observed in previous work, 43 where the dipole moment decreases from 1.87 to 1.81 D as the box size L increases from 10.58 Å toward infinity. We indeed observe a reduced dipole moment of 1.82

Table 1. AIMD Calculation Results for the Multipole Moments in the Local Frame on the Water Molecule

| | | \mathbf{e}_{x} | \mathbf{e}_{y} | \mathbf{e}_z |
|---------|----|------------------|------------------|----------------|
| monomer | P | 1.84 (1.86) | 0.00 | 0.00 |
| cavity | P | 2.70 | 0.00 | 0.00 |
| neat | P | 2.72 | 0.00 | 0.00 |
| | | | | |
| monomer | Q' | -0.13 (-0.13) | 2.56 (2.63) | -2.43(-2.50) |
| cavity | Q' | -0.15 | 3.13 | -2.98 |
| neat | Q' | -0.20 | 3.17 | -2.97 |
| | | | | |
| monomer | Q | -3.00 | -3.76 | -2.10 |
| cavity | Q | -2.83 | -1.92 | -3.95 |
| neat | Q | -2.81 | -1.90 | -3.94 |

""Monomer" indicates that there is a single water molecule in the simulation box. "Cavity" indicates that the moments are calculated in the liquid phase with a cavity of radius 4.1 Å at the simulation box center. "Neat" indicates that the calculations are performed for the pure water liquid phase. With the water oxygen atom as origin, the average values of the water molecular dipole moment P elements are in Debye (D) and the three average values of the diagonal elements of the water molecular primitive quadrupole moment Q are in D·Å. The average values of the off-diagonal elements are zero. Note that the average values of the magnitude of the dipole moment are 2.72 D for the cavity and 2.74 D for the neat liquid. With the center of mass of the water molecule as the origin, the three eigenvalues of the traceless quadrupole moment Q' are calculated in units of D·Å. The experimental values are shown in parentheses.

D when we calculate the dipole moment in a larger box of L = 16.00 Å.

In the neat liquid phase, we find that the average water atomic dipole moment is 5.77 D and the average water valence electronic dipole moment is -3.03 D, leading to the average water molecular dipole moment of 2.74 D. The increment of the water atomic dipole moment is 0.05 D, consistent with the observations⁴² that in the condensed phase, the average length of the O-H bond increases only slightly by 2.0% (0.02 Å) and the average H₁-O-H₂ angle increases slightly by 0.8%. This indicates that electronic polarization of water molecules in the liquid phase is primarily due to the decrease of the water valence electronic dipole moment in the interior bisector direction. The average dipole moment of water molecules within the cavity surface region is 2.72 D. In both calculations, our water molecular dipole moment calculations are in good agreement with the value of 2.70 D estimated by combining far-IR vibration—rotation—tunneling spectroscopy and ab initio calculations up to the large-cluster limit.⁴⁴

To compare with previous calculations for quadrupole moments, where the center of mass (COM) of the water molecule was chosen as the origin, the three eigenvalues of the traceless quadrupole moment for the water monomer are shown in Table 1, which agree well both with -0.13, 2.58, $-2.45~\rm D\cdot \mathring{A}$ as reported from DFT calculations³⁶ and with the experimental measurements⁴⁵ (in parentheses). For the water molecule in the condensed phase, our average eigenvalues over 60 000 configurations are in reasonable agreement with the previous DFT calculations³⁶ over 12 configurations: -0.22, 3.38, $-3.16~\rm D\cdot \mathring{A}$.

The primitive quadrupole moment of water shows in more detail how the water molecules are polarized by the neighboring molecules in the condensed phase. We calculate these elements in the water molecular local frame and with the

oxygen atom as the origin. Relative to the water monomer in vacuum, the less negative averages of Q_{xx} and Q_{yy} of water in the liquid suggest that the electron clouds of the neighboring molecules compress each other in these two directions. The more negative Q_{zz} indicates that the electron cloud gets stretched in the normal direction. Figure 1 exhibits how the

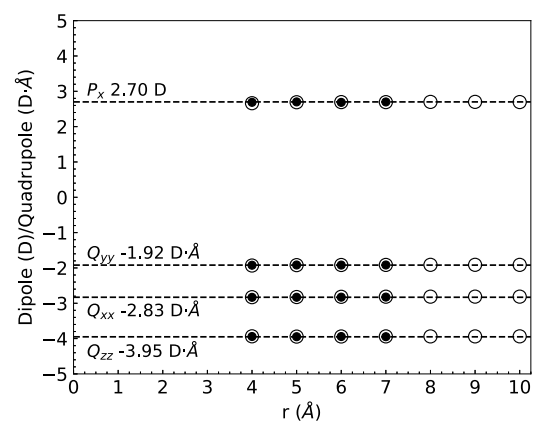


Figure 1. Average values of water multipole moments as a function of the distance from the cavity center. The average is over all the waters with the oxygen atom being located in a shell of size 1 Å. The open circles are for the DNN-MD calculation results, and the solid circles are the AIMD calculation results. The dashed lines are the average values over all of the waters in the whole cavity surface region. The DNN-MD and AIMD results are seen to be nearly identical.

average water molecular multipole-moments are nearly constant as a function of the distance from the cavity center. We see that the effect of the molecular-sized cavities on the water polarization is small.

After confirming accurate water dipole and quadrupole moments from the AIMD simulations, we stream the data into the DNN to train models for the moments, from which we can calculate the resulting electrostatic potential. In the DeepMD-kit framework, the accuracy is quantified in terms of the root-mean-square error. Our potential model gives an energy accuracy of 0.3 meV and a force accuracy of 56 meV/Å. The accuracy of the dipole moment is 0.04 D and that of the primitive quadrupole moment is 0.01 D·Å.

As shown in Figure 2, the excellent agreement of the atomic radial distribution functions (RDFs) between the DNN-MD and the AIMD trajectories suggests that the DNN-MD simulations accurately reproduce the structural properties of the liquid. The cavity center-oxygen RDF indicates that we can approach a bulk-like region at a distance of roughly 9.9 Å from the cavity center (with a cavity radius of 4.1 Å). Consequently, these results suggest that at least 256 waters are needed to provide a good bulk zero-reference for electrostatic potential calculations.

To assess the agreement between the computed DNN-MD moments and the AIMD-generated moments, we plot the distributions of dipole and quadrupole moments distributions in Figure 3. Note that, because the moment distributions in the lab frame should display no significant differences, we display the distributions of moment elements in the local coordinate system established as discussed above for the water monomer. The overlaps between the AIMD and DNN-MD distributions and the agreement of the average moment elements over a range of distances from the cavity center (as exhibited in Figure 1) allow us to explore the local potential contribution to

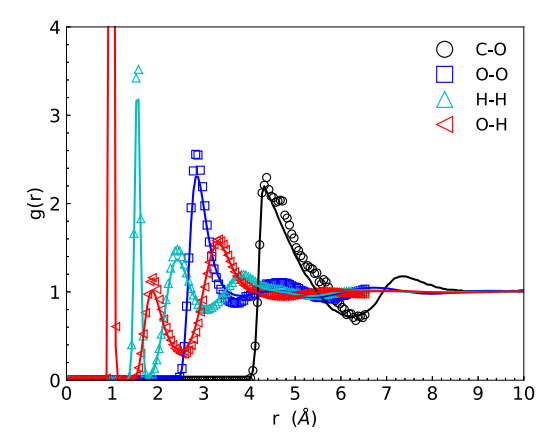


Figure 2. Radial distribution functions (RDFs) from AIMD and DNN-MD simulations. The circle symbols are for the RDF of the water oxygen atoms referenced to the cavity center from a 30 ps DFT simulation of 64 waters. The squares are for the DFT water oxygen—oxygen RDF; up-triangles are for the DFT hydrogen—hydrogen RDF, and the left-triangles are for the DFT oxygen—hydrogen RDF. The solid lines are from the DNN-MD (1000 ps) simulation of 256 waters.

the ion hydration free energy as carried out previously for the SPC/E classical model. 18

Table 2 presents results related to the various multipolar contributions to the local interfacial potential arising from nonuniform water molecule distributions near the cavity. We list the dipole moment contribution $\delta\phi_D$, the nonsymmetrical primitive moment contribution $\delta\phi_{Q2}$, and the symmetrical primitive moment contribution $\delta\phi_{Q1}$ for different systems. In the parentheses are the dipole and traceless quadrupole moment contributions using eq 19. Comparison of the results from the AIMD and DNN-MD simulations suggests that the DNN-MD model accurately reproduces the $\delta\phi_D$ and $\delta\phi_{Q2}$ contributions. Also, it is apparent that these two contributions obtain convergence within the first hydration shell ($r \leq 6.5$ Å). Referenced to the bulk phase of 256 waters, the simulation over 7.5 ns results in $\phi_{lp} = -3.96$ V (see Figure 4).

Finally, we utilize the above results and our previous study¹⁹ to compute the effective surface potential of water experienced by ions as they approach the interface. From data presented in

ref 19, the local potential in eq 5 can be obtained as an average of the difference between the interaction energies of the Na⁺ and F^- ions with the surrounding waters (Table 1 of ref 19.). For this calculation the water system is sampled with periodic boundary conditions (with the cavity present) but in the absence of interactions with the ions. Based on that average, the local potential is estimated to be -3.55 V. As a result of simulations for the ion—water interaction under the periodic boundary conditions, the Ewald-shift discussed above is thus estimated as -3.96 + 3.55 = -0.41 V. Considering the bulk solvation free energy of the Na⁺ ion reported as -92.8 kcal/ mol, 19 we estimate the intrinsic solvation free energy (all contributions except the surface potential in eq 5) as -184.0kcal/mol. The real solvation free energy of the Na+ ion (-101.5 kcal/mol) then implies a water liquid-vapor surface potential of 3.58 V. Therefore, the net potential is, as the sum of surface potential and local potential, $\phi_{\rm lp}$ + $\phi_{\rm sp}$ = -3.96 + 3.58 = -0.38 V, which is very close to our previous estimate.¹⁹ Note that there is a slight downward shift (of -0.07 to -0.08V) in the net potential for larger cavities (with radii of roughly 6 Å). See Table 2 and ref 18.

We make the following observations from the results presented above. First, the condensed phase water molecular dipole and quadrupole moments in the water local coordinate system are calculated, unraveling how the water molecule is polarized in the liquid phase. The physical effect is that the valence electron cloud is stretched along the normal direction to the water molecular plane, while the electron distribution is compressed in the other two orthogonal directions. Second, the deep neural network models reproduce the moments with good accuracy, indicating that this is a powerful tool to approach the environmental dependence of the multipole moments. This allows us to compute electrostatic potentials that play an important role in interfacial chemical phenomena. These calculations can be performed at low cost and with AIMD accuracy. This in turn allows for quantum-level modeling of interfacial processes that exceeds the previous AIMD limits in both size and time scales. Third, the surface potential is estimated as 3.58 V and the net potential as -0.38V, in agreement with previous AIMD results. 19 The results indicate the significant impact of periodic boundary conditions

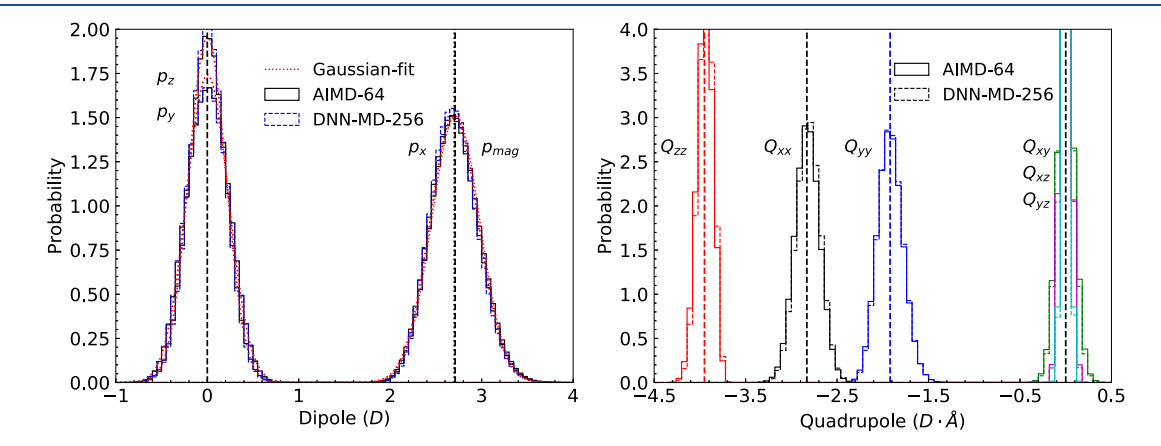


Figure 3. Distributions of water molecular dipole and quadrupole moments in the water molecular local frame. The solid lines are from 30 ps AIMD DFT simulations of 64 waters; the dashed lines are from 1000 ps DNN-MD simulations of 256 waters. The mean value (vertical dashed lines) and standard deviation (in the parentheses below) are from the AIMD DFT simulations. The dipole magnitudes are p_{mag} 2.72(0.26) D, p_x 2.70(0.26) D; p_y 0.00(0.20) D; p_z 0.00(0.23) D. The computed quadrupole moment tensor components are Q_{xx} -2.83 (0.14) D·Å, Q_{yy} -1.92(0.14) D·Å, Q_{xz} -3.95(0.09) D·Å, Q_{xy} -0.00(0.10) D·Å, Q_{xz} 0.00(0.05) D·Å, and Q_{yz} 0.00(0.04) D·Å. The red dotted line is the Gaussian distribution with the same mean and variance as obtained from the AIMD simulations.

Table 2. Moment Contributions to the Center Potential of a Cavity of Radius λ^a

| system | λ (Å) | running time (ps) | $r_{ m max}$ (Å) | $\delta\phi_{\scriptscriptstyle D}$ (V) | $\delta\phi_{\mathrm{Q2}}$ (V) | $\delta\phi_{Q1}\left(\mathrm{V} ight)$ |
|------------|-------|-------------------|------------------|---|--------------------------------|---|
| AIMD 64 | 4.10 | 30 | 6.50 | 0.22 (0.22) | 0.14 (0.11) | |
| DNN-MD 64 | 4.10 | 1000 | 6.50 | 0.24 (0.23) | 0.15 (0.12) | |
| DNN-MD 128 | 4.10 | 1000 | 8.00 | 0.23 (0.23) | 0.15 (0.12) | |
| DNN-MD 256 | 4.10 | 1000 | 9.90 | 0.23 (0.22) | 0.16 (0.13) | 3.60 |
| DNN-MD 256 | 4.10 | 7500 | 9.90 | 0.22 (0.22) | 0.16 (0.13) | 3.58 |
| DNN-MD 512 | 5.70 | 1000 | 12.60 | 0.30 (0.30) | 0.15 (0.12) | |

"Dipole moment contribution $\delta\phi_D$, non-symmetric quadrupole moment contribution $\delta\phi_{Q2}$, and Bethe potential contribution $\delta\phi_{Q1}$. In the parentheses are the dipole and traceless quadrupole moment contributions calculated using eq 19. The variable r_{max} is the upper limit of the cumulative summation of dipole and quadrupole contributions, for which the bin size is 0.1 Å.

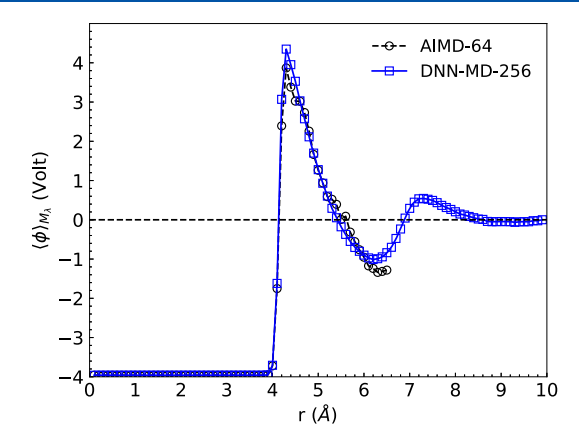


Figure 4. Cavity center potential $\langle \phi \rangle_{M_i} = -(\delta \phi_D + \delta \phi_{Q1} + \delta \phi_{Q2})$ as a function of distance from the center. The open circles are from 30 ps DFT simulations of 64 waters; the open squares are from DNN-MD 7500 ps simulations of 256 waters, for which $\delta \phi$ converges to 0 V at a distance of 9.9 Å.

on the computed ion solvation free energy calculation (the Ewald-shift discussed here). These effects should be included in simulation studies of the solvation of charged species using quantum mechanical methods.

COMPUTATIONAL METHODS

In the following section, we discuss the computational methods used to calculate the *ab initio* water molecular dipoles and primitive quadrupole moments in the liquid phase via AIMD simulations and DNN modeling. The DNN models allow for classical simulations on the nanosecond time scale.

Both the neat-water and cavity-water systems contain 64 waters at a water number density of $33.3285/\text{nm}^3$. Thus, the cubic simulation boxes are of size L=12.4295 Å and L=13.0236 Å (cavity size $\lambda=4.1$ Å), respectively. The cavity potential, $M_{\lambda}(r)$, is a half harmonic potential

$$M_{\lambda}(r) = \begin{cases} k(r - 1.05\lambda)^2 & r < 1.05\lambda \\ 0 & r \ge 1.05\lambda \end{cases}$$
(20)

where $k = 40 \text{ kcal/mol/Å}^2$.

For the two systems we perform DFT simulations by employing the Gaussian-type basis sets (DZVP-MOLOPT-SR-GTH) and plane wave (with 400 Ry cutoff)⁴⁶ and the Goedecker–Teter–Hutter (GTH)⁴⁷ pseudopotentials with the QuickStep module in the CP2K 2.6.1 package.⁴⁸ We use the revised Perdew, Burke, and Ernzerhof (revPBE) functional^{49,50} together with the Grimme D3 dispersion correction.^{51,52} A Nosé–Hoover thermostat⁵³ chain of length 3 is used to maintain a temperature of 330 K to increase the

fluidity and produce an oxygen—oxygen radial distribution function that agrees better with experiment.⁵⁴ Recent work has pointed out limitations in the usage of the higher temperatures alone in AIMD classical simulations aimed at modeling the detailed impact of nuclear quantum effects.^{55,56}

Electrostatic interactions under periodic boundary conditions are treated with the Ewald method. The simulations are run for 30 ps with a time step of 0.5 fs in the *NVT* ensemble, generating 60 000 configurations along with the total potential energy E and force on each atom \mathbf{F}_{ij} where i is the atom index. To calculate the MLWF we use the CRAZY method in the CP2K package with a convergence parameter of 10^{-8} .

In the DeePMD-kit framework,²⁵ a local coordinate frame should be constructed to preserve translational and rotational symmetry. Permutational symmetry is preserved by ordering neighboring atoms based on their species first and then by ordering based on increasing inverse distance from the atom of interest. We set up the local coordinate system (e_x', e_y', e_z') following the protocol from previous works.^{24,25} That is, e_x' is along the O-H bond, where atom H is the closest to the oxygen atom; $\mathbf{e}_{z'}$ is perpendicular to the plane of the water molecule, and $\mathbf{e}_{y'} = \mathbf{e}_{z'} \times \mathbf{e}_{x'}$. Within this local coordinate system, the descriptors are assembled for each atom, including the full radial and angular information for the first 24 oxygen atoms and 48 hydrogen atoms (the average number of neighboring oxygens in the first hydration shell around the empty cavity) and the radial information for the first 36 oxygen atoms and 72 hydrogen atoms within the cutoff radius $R_c = 6.0$ Å. After the first layer, the descriptors of each atom flow into a DNN of 5 hidden layers with decreasing number of neurons (240, 120, 60, 30, 10). This DNN maps the descriptors into the output layer, the *i*th atomic E_i .

The nonlinear activation function is taken to be the hyperbolic tangent. The forces on each atom are computed as the negative derivative with respect to position. The loss function is

$$L(p_{\epsilon}, p_{f}) = \frac{p_{\epsilon}}{N} \Delta E^{2} + \frac{p_{f}}{3N} \sum_{i} |\Delta F_{i}|^{2}$$
(21)

where ΔE and ΔF_i are the root-mean-square errors of the energy and forces; N is the number of atoms, and p_e and p_f are the adjustable prefactors. As the training proceeds, p_e begins at 0.02 and ends at 8, and p_f changes from 1000 to 1. The initial learning rate is 0.001 with a decay rate of 0.95 for 20 000 total decay steps. Loss function optimization is done using the Adam stochastic gradient descent method. The training data consists of energies and forces from AIMD simulations for both the neat-water and cavity-water systems. The batch-size is 4, and the training process goes for 4 000 000 steps. The AIMD simulations generate 120 000 frames, and from these we

build 20 data sets to train. After the model is sufficiently trained, model parameters are frozen. In this hybrid way, we obtain a more accurate DNN model for the molecular behavior near the cavity interface and in the bulk liquid phase.

In the AIMD simulations, the dipole and quadrupole moments are calculated in the lab frame with the oxygen atom as the origin. The fitting process is done in the local frame as required in DeepMD to preserve the symmetries. Then, using the rotation matrix and the oxygen atom position, we convert the fitting results back to the lab frame. Accordingly, modules were developed to fit the dipole vector and quadrupole tensor. The codes will be made freely available upon request to the authors following publication.

Recent developments of the DeePMD-kit package provide a module to train a DNN for the 12 coordinates of 4 Wannier centers (WC). Inspired by this work, we have developed modules to train a DNN for the 3 dipole components P_x , P_y , and P_z and a DNN for the 6 primitive quadrupole components, Q_{xxy} , Q_{xyy} , Q_{xyy} , Q_{yyz} , and Q_{zz} . The training process for each moment consists of 2 000 000 steps with a batch step of 5 and with all the other parameters kept the same as for the DNN for the potential energy.

The DeePMD-kit code provides LAMMPS⁵⁸ support through a third-party package in order to produce classical MD simulations that use the frozen DNN models to compute the atomic interactions. In this way, large time-scale classical simulations are accessible with quantum accuracy. We run NVT simulations in LAMMPS for systems of 64, 128, 256, and 512 waters with a cavity of radius 4.1 Å at the center. We apply the Nosé–Hoover thermostat with a chain of length 3 to maintain a temperature of 330 K. The system size is $L = \frac{1}{2}$

 $\left(\frac{N}{\rho} + \frac{4\pi}{3}r_c^3\right)^{1/3}$, where N is the water number, the number density is $\rho_W = 33.3285 \, (\text{nm})^{-3} \, (\text{or } 0.997 \, \text{g/cm}^3)$, and $r_c = 4.1 \,$ Å. The DNN-MD simulations are run for 1500 ps with the first 500 ps for equilibration and the subsequent 1000 ps for data production. The time step is 0.5 fs, and the trajectory is recorded every 0.01 ps (20 steps).

AUTHOR INFORMATION

Corresponding Author

Thomas L. Beck — Department of Chemistry, University of Cincinnati, Cincinnati, Ohio 45221-0172, United States; Present Address: National Center for Computational Sciences, Oak Ridge National Laboratory, Oak Ridge, TN 37830; orcid.org/0000-0001-8973-7145; Email: becktl@ucmail.uc.edu

Authors

Yu Shi — Department of Chemistry, University of Cincinnati, Cincinnati, Ohio 45221-0172, United States; [●] orcid.org/ 0000-0002-2538-0295

Carrie C. Doyle – Department of Chemistry, University of Cincinnati, Cincinnati, Ohio 45221-0172, United States

Complete contact information is available at: https://pubs.acs.org/10.1021/acs.jpclett.1c02328

Notes

The authors declare no competing financial interest.

ACKNOWLEDGMENTS

We acknowledge NSF grants CHE-1565632 and CHE-1955161 for financial support of this research. The computations were performed at the Ohio Supercomputer Center and the Advanced Research Computing Center in University of Cincinnati. Y.S. acknowledges the support of the College of Arts and Sciences at the University of Cincinnati.

REFERENCES

- (1) Sellner, B.; Valiev, M.; Kathmann, S. M. Charge and electric field fluctuations in aqueous NaCl electrolytes. *J. Phys. Chem. B* **2013**, *117*, 10869—10882.
- (2) Collins, K. D. Why continuum electrostatics theories cannot explain biological structure, polyelectrolytes or ionic strength effects in ion—protein interactions. *Biophys. Chem.* **2012**, *167*, 43—59.
- (3) Kunz, W.; Lo Nostro, P.; Ninham, B. The present state of affairs with Hofmeister effects. *Curr. Opin. Colloid Interface Sci.* **2004**, *9*, 1–18.
- (4) Lo Nostro, P.; Ninham, B. W. Hofmeister phenomena: an update on ion specificity in biology. *Chem. Rev.* **2012**, *112*, 2286–2322.
- (5) Cox, S. J.; Thorpe, D. G.; Shaffer, P. R.; Geissler, P. L. Assessing long-range contributions to the charge asymmetry of ion adsorption at the air—water interface. *Chemical science* **2020**, *11*, 11791–11800.
- (6) Cox, S. J.; Mandadapu, K. K.; Geissler, P. L. Quadrupole-mediated dielectric response and the charge-asymmetric solvation of ions in water. *J. Chem. Phys.* **2021**, *154*, 244502.
- (7) Matyushov, D. V. Nonlinear dielectric response of polar liquids. *J. Chem. Phys.* **2015**, *142*, 244502.
- (8) Lee, M.-S.; Singer, S. J. Dielectric Behavior near a Spherical Ion. *J. Phys. Chem. B* **2021**, *125*, 2360–2371.
- (9) Beck, T. L. A local entropic signature of specific ion hydration. *J. Phys. Chem. B* **2011**, *115*, 9776–9781.
- (10) Ashbaugh, H. S.; Asthagiri, D. Single ion hydration free energies: A consistent comparison between experiment and classical molecular simulation. *J. Chem. Phys.* **2008**, *129*, 204501.
- (11) Shi, Y.; Beck, T. L. Length scales and interfacial potentials in ion hydration. *J. Chem. Phys.* **2013**, *139*, 044504.
- (12) Beck, T. L.; Paulaitis, M. E.; Pratt, L. R. The Potential Distribution Theorem and Models of Molecular Solutions; Cambridge University Press, 2006.
- (13) Asthagiri, D.; Dixit, P.; Merchant, S.; Paulaitis, M.; Pratt, L.; Rempe, S. B.; Varma, S. Ion selectivity from local configurations of ligands in solutions and ion channels. *Chem. Phys. Lett.* **2010**, 485, 1–7.
- (14) Weber, V.; Merchant, S.; Asthagiri, D. Communication: Regularizing binding energy distributions and thermodynamics of hydration: Theory and application to water modeled with classical and ab initio simulations. *J. Chem. Phys.* **2011**, *135*, 181101.
- (15) Pollard, T.; Beck, T. L. Quasichemical Analysis of the Cluster Pair Approximation for the Thermodynamics of Proton Hydration. *J. Chem. Phys.* **2014**, *140*, 224507.
- (16) Pollard, T. P.; Beck, T. L. The Thermodynamics of Proton Hydration and the Electrochemical Surface Potential of Water. *J. Chem. Phys.* **2014**, *141*, 18C512.
- (17) Pollard, T. P.; Beck, T. L. Toward a Quantitative Theory of Hofmeister Phenomena: From Quantum Effects to Thermodynamics. *Curr. Opin. Colloid Interface Sci.* **2016**, *23*, 110–118.
- (18) Doyle, C. C.; Shi, Y.; Beck, T. L. The Importance of the Water Molecular Quadrupole for Estimating Interfacial Potential Shifts Acting on Ions Near the Liquid-Vapor Interface. *J. Phys. Chem. B* **2019**, *123*, 3348–3358. PMID: 30920221
- (19) Shi, Y.; Beck, T. L. Absolute ion hydration free energy scale and the surface potential of water via quantum simulation. *Proc. Natl. Acad. Sci. U. S. A.* **2020**, *117*, 30151–30158.
- (20) Ashbaugh, H. S. Convergence of molecular and macroscopic continuum descriptions of ion hydration. *J. Phys. Chem. B* **2000**, *104*, 7235–7238.

- (21) Conboy, J. C.; Richmond, G. L. Examination of the Electrochemical Interface Between Two Immiscible Electrolyte Solutions by Second Harmonic Generation. *J. Phys. Chem. B* **1997**, *101*, 983–990.
- (22) Mishra, H.; Enami, S.; Nielsen, R. J.; Stewart, L. A.; Hoffmann, M. R.; Goddard, W. A.; Colussi, A. J. Brønsted Basicity of the Air—Water Interface. *Proc. Natl. Acad. Sci. U. S. A.* **2012**, *109*, 18679—18683.
- (23) Lee, J. K.; Walker, K. L.; Han, H. S.; Kang, J.; Prinz, F. B.; Waymouth, R. M.; Nam, H. G.; Zare, R. N. Spontaneous generation of hydrogen peroxide from aqueous microdroplets. *Proc. Natl. Acad. Sci. U. S. A.* **2019**, *116*, 19294–19298.
- (24) Zhang, L.; Han, J.; Wang, H.; Car, R.; Weinan, E. Deep potential molecular dynamics: a scalable model with the accuracy of quantum mechanics. *Phys. Rev. Lett.* **2018**, *120*, 143001.
- (25) Wang, H.; Zhang, L.; Han, J.; Weinan, E. DeePMD-kit: A deep learning package for many-body potential energy representation and molecular dynamics. *Comput. Phys. Commun.* **2018**, 228, 178–184.
- (26) Zhang, L.; Lin, D.-Y.; Wang, H.; Car, R.; E, W. Active learning of uniformly accurate interatomic potentials for materials simulation. *Phys. Rev. Materials* **2019**, *3*, 023804.
- (27) Zhang, L.; Chen, M.; Wu, X.; Wang, H.; E, W.; Car, R. Deep neural network for the dielectric response of insulators. *Phys. Rev. B: Condens. Matter Mater. Phys.* **2020**, *102*, 041121.
- (28) Jia, W.; Wang, H.; Chen, M.; Lu, D.; Lin, L.; Car, R.; Weinan, E.; Zhang, L. Pushing the Limit of Molecular Dynamics with Ab Initio Accuracy to 100 Million Atoms with Machine Learning. SC20: International Conference for High Performance Computing, Networking, Storage and Analysis; 2020; pp 1–14.
- (29) Horváth, L.; Beu, T.; Manghi, M.; Palmeri, J. The vapor-liquid interface potential of (multi)polar fluids and its influence on ion solvation. *J. Chem. Phys.* **2013**, *138*, 154702.
- (30) Remsing, R. C.; Baer, M. D.; Schenter, G. K.; Mundy, C. J.; Weeks, J. D. The Role of Broken Symmetry in Solvation of a Spherical Cavity in Classical and Quantum Water Models. *J. Phys. Chem. Lett.* **2014**, *5*, 2767–2774. PMID: 26278076
- (31) Wolfgang Schmickler, E. S. *Interfacial Electrochemistry*; Oxford University Press: Oxford, 1996.
- (32) Fawcett, W. R. Liquid, Solutions, and Interfaces: from Classical Macroscopic Descriptions to Modern Microscopic Details; Oxford: New York, 2004.
- (33) Wilson, M. A.; Pohorille, A.; Pratt, L. R. Comment on "Study on the liquid–vapor interface of water. I. Simulation results of thermodynamic properties and orientational structure. *J. Chem. Phys.* **1989**, *90*, 5211–5213.
- (34) Hummer, G.; Pratt, L. R.; García, A. E. Free Energy of Ionic Hydration. *J. Phys. Chem.* **1996**, *100*, 1206–1215.
- (35) Duignan, T. T.; Baer, M. D.; Schenter, G. K.; Mundy, C. J. Electrostatic solvation free energies of charged hard spheres using molecular dynamics with density functional theory interactions. *J. Chem. Phys.* **2017**, *147*, 161716.
- (36) Silvestrelli, P. L.; Parrinello, M. Structural, electronic, and bonding properties of liquid water from first principles. *J. Chem. Phys.* **1999**, *111*, 3572–3580.
- (37) Wan, Q. First Principles Simulations of Vibrational Spectra of Aqueous Systems. Ph.D. Thesis, University of Chicago, 2015.
- (38) Zhang, L.; Chen, M.; Wu, X.; Wang, H.; Weinan, E.; Car, R. Deep neural network for the dielectric response of insulators. *Phys. Rev. B: Condens. Matter Mater. Phys.* **2020**, *102*, 041121.
- (39) Sommers, G. M.; Andrade, M. F. C.; Zhang, L.; Wang, H.; Car, R. Raman spectrum and polarizability of liquid water from deep neural networks. *Phys. Chem. Chem. Phys.* **2020**, 22, 10592–10602.
- (40) Batista, E. R.; Xantheas, S. S.; Jónsson, H. Molecular multipole moments of water molecules in ice Ih. *J. Chem. Phys.* **1998**, *109*, 4546–4551.
- (41) Clough, S. A.; Beers, Y.; Klein, G. P.; Rothman, L. S. Dipole moment of water from Stark measurements of H2O, HDO, and D2O. *J. Chem. Phys.* **1973**, *59*, 2254–2259.

- (42) Silvestrelli, P. L.; Parrinello, M. Water Molecule Dipole in the Gas and in the Liquid Phase. *Phys. Rev. Lett.* **1999**, 82, 3308–3311.
- (43) Sagui, C.; Pomorski, P.; Darden, T. A.; Roland, C. Ab initio calculation of electrostatic multipoles with Wannier functions for large-scale biomolecular simulations. *J. Chem. Phys.* **2004**, *120*, 4530–4544.
- (44) Gregory, J. K.; Clary, D. C.; Liu, K.; Brown, M. G.; Saykally, R. J. The Water Dipole Moment in Water Clusters. *Science* **1997**, 275, 814–817.
- (45) Verhoeven, J.; Dymanus, A. Magnetic Properties and Molecular Quadrupole Tensor of the Water Molecule by Beam-Maser Zeeman Spectroscopy. *J. Chem. Phys.* **1970**, *52*, 3222–3233.
- (46) VandeVondele, J.; Hutter, J. Gaussian basis sets for accurate calculations on molecular systems in gas and condensed phases. J. Chem. Phys. 2007, 127, 114105.
- (47) Goedecker, S.; Teter, M.; Hutter, J. Separable dual-space Gaussian pseudopotentials. *Phys. Rev. B: Condens. Matter Mater. Phys.* **1996**, 54, 1703–1710.
- (48) Vandevondele, J.; Sprik, M. A molecular dynamics study of the hydroxyl radical in solution applying self-interaction-corrected density functional methods. *Phys. Chem. Chem. Phys.* **2005**, *7*, 1363–1367.
- (49) Perdew, J. P.; Burke, K.; Ernzerhof, M. Generalized Gradient Approximation Made Simple. *Phys. Rev. Lett.* **1996**, *77*, 3865–3868.
- (50) Zhang, Y.; Yang, W. Comment on "Generalized Gradient Approximation Made Simple". *Phys. Rev. Lett.* **1998**, *80*, 890–890.
- (51) Grimme, S. Accurate description of van der Waals complexes by density functional theory including empirical corrections. *J. Comput. Chem.* **2004**, *25*, 1463–1473.
- (52) Grimme, S.; Antony, J.; Ehrlich, S.; Krieg, H. A consistent and accurate ab initio parametrization of density functional dispersion correction (DFT-D) for the 94 elements H-Pu. *J. Chem. Phys.* **2010**, 132, 154104.
- (53) Martyna, G.; Klein, M.; Tuckerman, M. Nosé-Hoover chains: The canonical ensemble via continuous dynamics. *J. Chem. Phys.* **1992**, *97*, 2635–2643.
- (54) Morrone, J. A.; Car, R. Nuclear quantum effects in water. *Phys. Rev. Lett.* **2008**, *101*, 017801.
- (55) Ceriotti, M.; Fang, W.; Kusalik, P. G.; McKenzie, R. H.; Michaelides, A.; Morales, M. A.; Markland, T. E. Nuclear quantum effects in water and aqueous systems: Experiment, theory, and current challenges. *Chem. Rev.* **2016**, *116*, 7529–7550.
- (56) Li, C.; Paesani, F.; Voth, G. A. Classical Ab Initio Molecular Dynamics Run at an Elevated Temperature is Not a Good Model for the Nuclear Quantum Effects in Water at Ambient Temperature. *ChemRxiv.org* **2021**. DOI: 10.33774/chemrxiv-2021-c603x
- (57) Kingma, D. P.; Ba, J. Adam: A method for stochastic optimization. arXiv 2014, 1412.6980.
- (58) Brown, W. M.; Kohlmeyer, A.; Plimpton, S. J.; Tharrington, A. N. Implementing molecular dynamics on hybrid high performance computers—Particle—particle particle-mesh. *Comput. Phys. Commun.* **2012**, *183*, 449–459.